

Resolution dependency of sinking Lagrangian particles in ocean general circulation models

Peter D. Nooteboom^{1,2*}, Philippe Delandmeter¹, Erik van Sebille^{1,2}, Peter K. Bijl³, Henk A. Dijkstra^{1,2}, Anna S. von der Heydt^{1,2}

1 Institute for Marine and Atmospheric research Utrecht (IMAU), Department of Physics, Utrecht University, Utrecht, Netherlands

2 Centre for Complex Systems Studies, Utrecht University, Utrecht, Netherlands

3 Laboratory of Paleobotany and Palynology, Department of Earth Sciences, Utrecht University, Utrecht, Netherlands

* p.d.nooteboom@uu.nl

Abstract

Any type of non-buoyant material in the ocean is transported horizontally by currents during its sinking journey. This lateral transport can be far from negligible for small sinking velocities. To estimate its magnitude and direction, the material is often modelled as a set of Lagrangian particles advected by current velocities that are obtained from Ocean General Circulation Models (OGCMs). State-of-the-art OGCMs are strongly eddying, similar to the real ocean, providing results with a spatial resolution on the order of 10 km on a daily frequency. While the importance of eddies in OGCMs is well-appreciated in the physical oceanographic community, other marine research communities may not. Further, many long term climate modelling simulations (e.g. in paleoclimate) rely on lower spatial resolution models that do not capture mesoscale features. To demonstrate how much the absence of mesoscale features in low-resolution models influences the Lagrangian particle transport, we simulate the transport of sinking Lagrangian particles using low- and high-resolution global OGCMs, and assess the lateral transport differences resulting from the difference in spatial and temporal model resolution. We find major differences between the transport in the non-eddy OGCM and in the eddy OGCM. Addition of stochastic noise to the particle trajectories in the non-eddy OGCM parameterises the effect of eddies well in some cases (e.g. in the North Pacific gyre). The effect of a coarser temporal resolution (once every 5 days versus monthly) is smaller compared to a coarser spatial resolution (0.1° versus 1° horizontally). We recommend to use sinking Lagrangian particles, representing e.g. marine snow, microplankton or sinking plastic, only with velocity fields from eddy Eulerian OGCMs, requiring high-resolution models in e.g. paleoceanographic studies. To increase the accessibility of our particle trace simulations, we launch planktondrift.science.uu.nl, an online tool to reconstruct the surface origin of sedimentary particles in a specific location.

Introduction

Sinking particles are involved in fundamental processes in the ocean. They serve as a primary mode of carbon export out of the exogenic carbon pool and deliver sediment to the world ocean floor: An important archive for understanding the climate system. The

lateral advection of the sinking particles by ocean currents complicates the estimation of downward particle fluxes captured by sediment traps [5], the paleoceanographic reconstructions based on sedimentary microplankton distributions [6–9], and the estimation of micro-plastic distributions in the ocean [10]. Initially buoyant micro-plastic in the ocean sinks when it gets biofouled and its density increases [11], meaning that a large fraction of the plastic in the ocean has already sunk to the ocean floor [12]. The lateral transport of sinking particles can be estimated using Ocean General Circulation Models (OGCMs) and Lagrangian tracking techniques [13]. The Lagrangian techniques are used to model the sinking particle trajectories in the modern ocean [14–18, 57], specifically for sinking microplankton [19, 20] and microplastic [21].

Where possible, these Lagrangian techniques make use of an eddying flow field. However, eddying simulations are not available for all applications to provide such a flow field. For example, model simulations of the geological past use OGCMs with at most 1° horizontal (non-eddying) resolution [22–26]. The latter is due to the fact that palaeoclimate model simulations require coupled climate model simulations (because the atmospheric forcing is not known from observations) and long spin-up times (typically a few 1000 model years) in order to reach a reasonable climate equilibrium.

The spatial and temporal resolution of the underlying flow field generated by OGCMs will affect the spreading of particles in the Lagrangian tracking. It has already been shown that Lagrangian trajectories of neutrally buoyant particles are sensitive to the temporal resolution in an OGCM with $\sim 2^\circ$ horizontal resolution [27], and the temporal resolution influences the divergence timescale of trajectories in an OGCM of 0.1° horizontal resolution [28].

The spatial resolution of the OGCM determines if the flow is eddying, which played an important role in simulations of sinking particles near the northern Gulf of Mexico [29] and in the Benguela region [17], and for passive tracers near Sellafield [59] and globally [58] (0.25° versus 1° resolution). Eddying OGCMs generate a different time-mean flow compared to non-eddying OGCMs which parameterise the eddy effects [30, 31]. The interplay between eddies and the mean flow is found to be important for the representation of internal variability of the flow (i.e. the variability of the system under constant atmospheric forcing) [32]. This results in a better representation of interannual or multidecadal variability [33] and the separation location of western boundary currents such as the Gulf Stream [34]. Additionally, eddies cause mixing of tracers (e.g. heat and salinity). The non-eddying OGCMs rely on parameterisations of this tracer mixing such as the Gent-McWilliams (GM) parameterisation [35, 36], which shows difficulties to represent this effect locally [37, 38].

In this paper, we will assess how the sinking Lagrangian particle trajectories vary for different temporal or spatial resolutions of an Eulerian OGCM. We investigate the effect of eddies on the particle trajectories. Moreover, we study whether a stochastic lateral diffusion of Smagorinsky [39] type could parameterise the effects of the eddies in the non-eddying OGCM. We use the same analysis as is applied in [20] about microplankton which is used for palaeoceanographic reconstruction (specifically dinoflagellate cysts). The results concern any type of application with sinking Lagrangian particles, such as the comparison of sediment trap data with OGCMs [29, 57] or the representation of sinking microplankton [19, 20] and sinking plastic [11].

We disseminate our results further with an interactive website:

<https://www.planktondrift.science.uu.nl>. This online tool simulates the surface origin of particles that sink to the bottom of the present-day ocean. The tool can also be used to determine how the microplankton in the bottom sediments at any location of choice relates to the environment at these origin locations (e.g. temperature, salinity, primary productivity) in the present-day ocean (see also [20]).

Method

We make use of present-day global ocean model simulations of the Parallel Ocean Program (POP) with 0.1° ($R_{0.1}$; eddying) and 1° (R_{1m} ; non-eddying) horizontal resolution to advect virtual particles (also used in [38, 40, 41]). The eddying POP version has a reasonably good representation of the modern circulation compared to other models at the same resolution [64]. Both versions of POP are configured to be as consistent as possible with each other, but there are some differences (see the supplementary material of [40]).

We apply the same particle tracking approach as in [20]. This means that we release particles at the bottom of the ocean every three days for more than a year, and compute their trajectories in the changing flow field back in time (similar to [13, 20, 29, 57]) until the particles reached the surface. We stop a particle if it reaches 10m depth. The particles are released on a $1^\circ \times 1^\circ$ global grid. The resulting particle distributions allow us to investigate the statistics of particle ensembles, rather than single trajectories. Particle ensemble statistics are often used in Lagrangian analysis [13], because of the chaotic nature of the particle trajectories [65]. While the particles are advected back in time, a constant sinking velocity w_f is added to the particle trajectories. The addition of a constant sinking velocity to an advected particle has been shown to be a proper way to incorporate the effect of gravity on a sinking particle [42]. We used Parcels version 2.0.0 [43] to calculate the particle trajectories, which is compatible with the Arakawa B-grid that POP uses.

The sinking velocity of particles in the ocean varies substantially. The sinking speed w_f of microplastics is on the order of $3.4\text{--}50 \text{ m day}^{-1}$ [12], for single dinoflagellate cysts w_f ranges from $6 - 11 \text{ m day}^{-1}$ [44], and the sinking speed can become several hundreds of meters per day for marine snow aggregates (e.g. $10\text{--}287 \text{ m day}^{-1}$ [45]). The larger w_f , the shorter the travel time of the particles will be and the less the particle distributions at the surface will spread. Here, we focus on two sinking speeds: $w_f = 6$ and 25 m day^{-1} , to study the dependence of the results on the sinking speed, i.e. we represent the sinking of individual dinoflagellate cysts and small aggregates, respectively. More scenarios of sinking speed w_f were investigated in [20].

The particle trajectory is integrated using the velocity field of POP and a stochastic term parameterising the effect of unresolved processes on the velocity. This last term is equivalent to diffusion in Eulerian models [13] and is a function of the diffusivity ν . Here we define ν as a function of the mesh size (i.e. the size of the grid cell) and the flow shear, following the Smagorinsky [39] parameterisation, which is commonly used in OGCMs and Large Eddy Simulations (LES). This implies that the particle trajectories are computed by:

$$\vec{x}(t - \Delta t) = \vec{x}(t) + \int_t^{t-\Delta t} \vec{v}(\vec{x}, \tau) d\tau + \vec{c}\Delta t + \vec{q}\sqrt{2\nu(\vec{x})\Delta t}, \quad (1)$$

with $\vec{x}(t)$ the three-dimensional position of the particle at time t , $\vec{v}(\vec{x}, t)$ the flow velocity at location \vec{x} and time t (linearly interpolated in space and time from the flow field), and $\vec{c} = (0 \quad 0 \quad -w_f)^T$ the sinking velocity. The vertical part of the flow \vec{v} can be relevant compared to the particle sinking velocity w_f (see Fig 7 in [20]). The flow consists of two components in the non-eddying POP model: $\vec{v} = \vec{v}_a + \vec{v}_b$, where \vec{v}_a is the Eulerian flow field that is solved by POP. \vec{v}_b is the bolus velocity from the GM parameterisation, which represents the flow that is responsible for the mixing of tracers along isopycnals [35, 36]. $\vec{v}_b = \vec{0}$ in the eddying POP model.

The last term of Eq. 1 is the horizontal diffusivity term (only used in the non-eddying model), where $\vec{q} = (R_1 \quad R_2 \quad 0)^T$ represents (independent) white noise in the zonal and meridional direction, with mean $\mu_{R_1} = \mu_{R_2} = 0$ and variance

$\sigma_{R_1}^2 = \sigma_{R_2}^2 = 1$, and

$$\nu(\vec{x}) = c_s A \sqrt{\left(\frac{\partial u}{\partial x}\right)^2 + \frac{1}{2} \left(\frac{\partial u}{\partial y} + \frac{\partial v}{\partial x}\right)^2 + \left(\frac{\partial v}{\partial y}\right)^2}, \quad (2)$$

where A is the horizontal surface area of the grid cell where the particle is located, $u = u(\vec{x})$ and $v = v(\vec{x})$ are respectively the (depth dependent) zonal and meridional velocity components. As such, the magnitude of the stochastic noise depends on the local velocity field, and its variance increases linearly over the time that a particle is advected. The Smagorinsky viscosity depends strongly on the flow shear compared to other parameterisations [46].

The strength of the noise can be determined with the parameter $c_s \geq 0$. Multiple methods exist in LES to determine the value of c_s in each application [47]. The velocity gradients $\left(\frac{\nu}{c_s A}\right)$ in the non-eddying version of POP typically range from 10^{-9}s^{-1} to 10^{-7}s^{-1} and $A \approx 10^4 \text{ km}^2$, so the estimated standard deviation of the zonal and meridional stochastic noise ($\hat{\sigma}_x(t)$, $\hat{\sigma}_y(t)$) after 20 days ($\Delta t \approx 1.6 \cdot 10^6\text{s}$) range from $6\sqrt{c_s}$ km to $60\sqrt{c_s}$ km. These scales are similar to the mesoscale: 10-30 days and 10-100km for mesoscale eddies [48].

Altogether, we apply the particle tracking analysis in four different model configurations (see Table 1), and compare the distributions of particles at the ocean surface after the back-tracking from a single release location; 130 particles are used at every release location to determine the particle distributions. These configurations represent the differences between state-of-the-art, global OGCM resolutions of the past (1° horizontally and monthly model output) and the present-day (0.1° horizontally and model output on a daily scale). The single effect of model output with lower temporal resolution compared to the state-of-the-art present-day OGCMs is investigated in a separate configuration $R_{0.1m}$.

Table 1. The configurations with simulations in varying OGCM resolutions

Configuration	resolution	output	diffusion	remark
$R_{0.1}$	0.1°	once every 5 days	$c_s = 0$	Reference case, $\vec{v}_b = 0$, eddying
$R_{0.1m}$	0.1°	monthly	$c_s = 0$	$\vec{v}_b = \vec{0}$, eddying
R_{1m}	1°	monthly	$c_s = 0$	non-eddying
R_{1md}	1°	monthly	$c_s \in [0.25, 0.5, 1.0, 1.5, 2.0, 5.0]$	non-eddying

We use three measures to compare the particle distributions between the configurations (see Fig 1b-d): (i) the average lateral distance (km) travelled from the release location (along the red lines in Fig 1b), (ii) the surface area spanned by the particles approximated by the summed surface area of the $1^\circ \times 1^\circ$ grid boxes (blue boxes in Fig 1c), and (iii) the Wasserstein distance W_d as a measure of difference between two distributions resulting from two simulations. The Wasserstein distance is the minimum distance that one has to displace the particles resulting from one simulation (along the dashed lines in Fig 1d) to transform it into another particle distribution (and is calculated with [49]).

Results

We first analyse the overall differences between the configurations $R_{0.1m}$, R_{1m} , R_{1md} and the reference configuration $R_{0.1}$ in terms of the three measures described above (see Fig 1). Thereafter, we show specific release locations to explain why the configurations

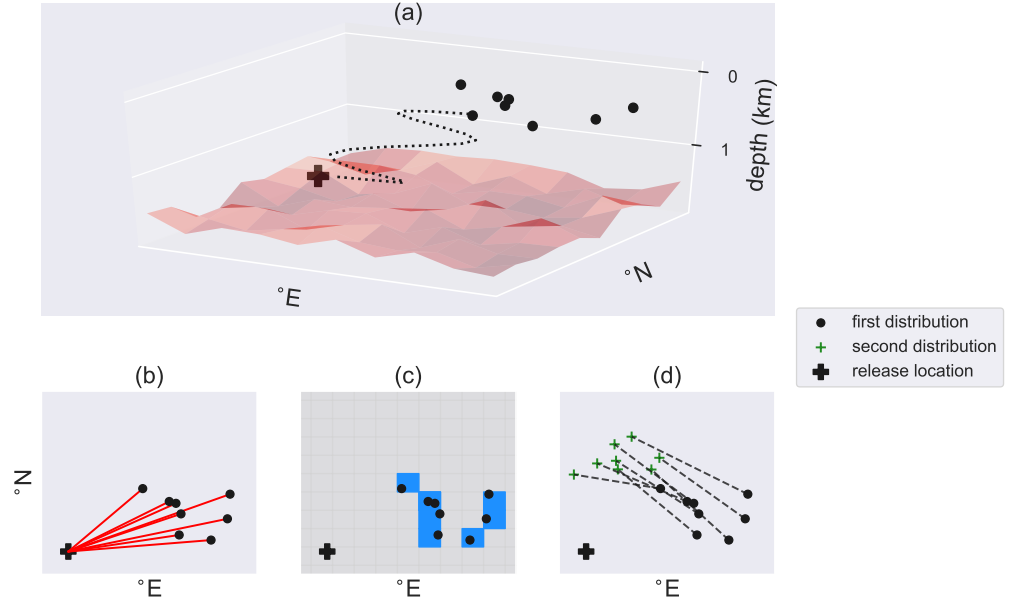


Fig 1. Schematic illustration of (a) the back-tracking analysis and (b)-(d) the three measures which are used to compare the particle distributions at the ocean surface. (a) Three-dimensional illustration: Particles are released at the bottom every three days for a period of around six years, back-tracked until they get close to the surface (10m depth), which results in a particle distribution at the surface. A map of (b) the average lateral distance (km) traveled from the release location (along the red lines), (c) the surface area (blue; km^2) spanned by the particle distribution (approximated by the summed surface area of the $1^\circ \times 1^\circ$ blue boxes), (d) the Wasserstein distance (W_d ; km), which is the minimum distance that one has to displace the particles (along the dashed lines) to transform one distribution into another distribution.

with lower spatial resolution do or do not provide similar solutions to the reference configuration $R_{0.1}$.

Global analysis

The average lateral travel distances of the particles are globally different between the four configurations (Fig 2). In the configuration with lower spatial resolution R_{1m} , the average lateral displacement is more extreme compared to the reference configuration (i.e. it is larger in regions with relatively large displacement and lower in regions with low displacement; Fig 2c). The average travel distance in $R_{0.1m}$ is similar to the reference case $R_{0.1}$ (see Fig 2d for the global averages).

The average lateral displacement becomes globally less ‘extreme’ (especially the Southern Ocean peaks are lower) if the Smagorinsky diffusion is added to the flow dynamics in R_{1md} compared to R_{1m} (Fig 2c). The less extreme pattern of the travel distances explains why the globally averaged lateral travel distance is minimal at $c_s = 0.25$ (for $w_f = 6 \text{ m day}^{-1}$ in Fig 2d), and not at $c_s = 0$. The coefficient c_s influences the lateral displacement in two ways. First, more displacement is added per time step if the noise is stronger (for larger c_s), and the lateral displacement will on average be larger for larger c_s . Second, the noise will be larger in areas with strong flow (u and v in Eq. 1 and 2). Hence, for small c_s the noise is large enough for the particles to travel outside of the areas with a relatively strong flow and large displacement (such

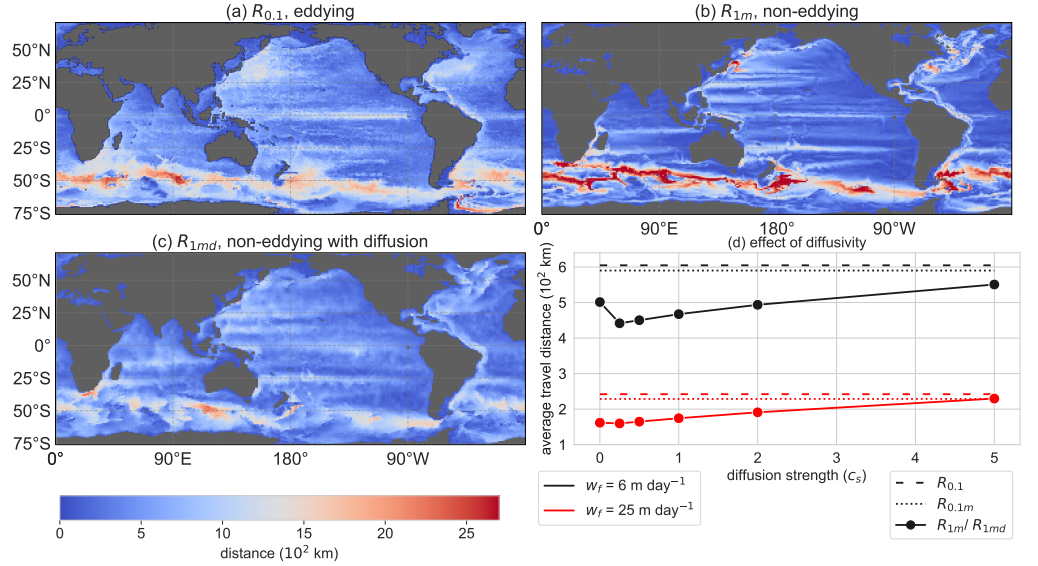


Fig 2. (a), (b), (c) The average horizontal distance between the release location and the final back-tracked location at the ocean surface with $w_f = 6 \text{ m day}^{-1}$ respectively in configuration $R_{0.1}$, R_{1m} , R_{1md} with diffusion strength $c_s = 2.0$ (see Fig 4 for $R_{0.1m}$). (d) Global averaged lateral travel distance in all configurations (for several values of c_s in R_{1md}). $w_f = 6 \text{ m day}^{-1}$ in black and $w_f = 25 \text{ m day}^{-1}$ in red.

as in the Southern Ocean), such that the globally averaged lateral displacement is lower than for $c_s = 0$.

The surface area spanned by the particle distributions (1b) is often smaller in $R_{0.1m}$ compared to $R_{0.1}$, as can be seen from the global average of this measure (Fig 3d). The lower surface area could be explained by the tendency of nearby particles to follow more similar pathways in $R_{0.1m}$ than in $R_{0.1}$ (see animation S3 in the supporting material) [28]. As a result, the particles will end up in clusters closer to each other at the surface. Hence, the surface area of the particle distributions is on average smaller in $R_{0.1m}$ compared to $R_{0.1}$.

Mesoscale eddies are abundant in the reference configuration $R_{0.1}$, while they are absent in the low spatial resolution configuration R_{1m} . Therefore, tracked particles tend to end up in a much more confined area at the surface in the lower resolution configuration R_{1m} than in the reference configuration (Fig 3d). The stochastic noise in R_{1md} induces fluctuations in the particle trajectories, leading to a larger surface area of the particle distributions. In R_{1md} , the global average surface area of the particle distributions increases monotonically with increasing magnitude of the noise (c_s).

Interestingly, the value of c_s that approximates configuration $R_{0.1}$ ($c_s \approx 3.5$) and $R_{0.1m}$ ($c_s \approx 2$) best, is the same for both sinking velocities $6, 25 \text{ m day}^{-1}$. These values of c_s must result in a similar scale of the flow fluctuations (σ_x, σ_y) in configurations $R_{0.1}$ and $R_{0.1m}$. It also indicates that, given c_s , the subgrid-scale parameterisation performance is similar for both sinking velocities. Nevertheless, the particle distributions match better with the reference configuration if the sinking velocity is higher (according to the W_d in Fig 2), because a lower particle travel time leads to less spread of the particle trajectories and a lower lateral displacement.

Locally, the surface area of the particle distributions shows a different pattern in R_{1md} compared to the reference $R_{0.1}$ (Fig 3a vs c). In contrast to the magnitude of the noise, the direction of the noise vector does not depend on the flow field (it is horizontally isotropic). Therefore, the surface area of the particle distributions in

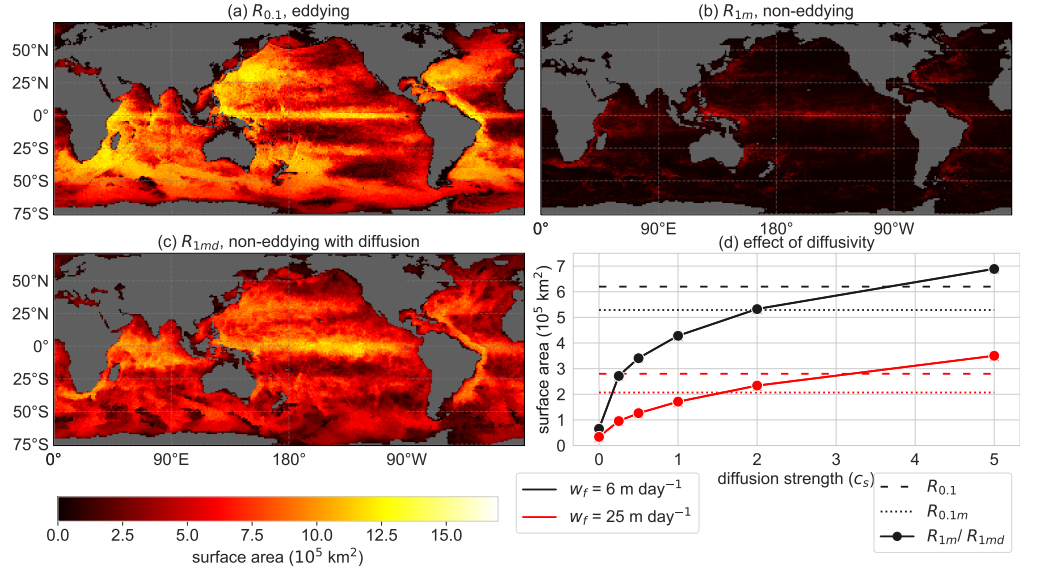


Fig 3. (a), (b), (c) The surface area of the back-tracked particle distributions with $w_f = 6 \text{ m day}^{-1}$ respectively in configuration $R_{0,1}$, R_{1m} , R_{1md} with diffusion strength $c_s = 2.0$ (see Fig 5 for $R_{0,1m}$). (d) Globally averaged surface area of the particle distributions in all configurations (for several values of c_s in R_{1md}). $w_f = 6 \text{ m day}^{-1}$ in black and $w_f = 25 \text{ m day}^{-1}$ in red.

configuration R_{1md} is overestimated in the tropics compared to the reference configuration $R_{0,1}$, where the flow is mostly zonal. Interestingly, this measure remains low in areas with sinking waters for both configurations $R_{0,1}$ and $R_{0,1md}$, such as the Ross sea and the Weddell sea (see Fig 2 in [66]).

The loss of information in $R_{0,1m}$ due to the monthly averaging of the flow fields in $R_{0,1}$ is clearer in the difference plots of the surface area and travel distance of the particle distributions (Fig 4). The surface area of the particle distributions is mostly lower in $R_{0,1m}$ compared to $R_{0,1}$ (Fig 4a). The particles tend to be advected by a similar flow field in $R_{0,1m}$ if they are located close to each other. Hence, groups of particles are trapped in the same eddies, and travel from origin locations at the ocean surface which are closer to each other. This could result in notably different back-tracked particle distributions, especially if the shear of the flow field is high (see for instance the location 45.5°S , 39.5°E on planktondrift.science.uu.nl or Fig S1 for two similar locations with opposite behaviour).

In general, we find that a reduction of the temporal resolution ($R_{0,1m}$ vs. the reference case $R_{0,1}$) does not have a major effect on the Wasserstein distance W_d (Fig 5). The travel time of the particles is perhaps too short (at most a few years) for the errors in $R_{0,1m}$ to grow substantially, and remains smaller compared to R_{1m} . The global average W_d between $R_{0,1m}$ and the reference case ($W_d(R_{0,1}, R_{0,1m})$) is slightly larger compared to the check of $R_{0,1}$ with itself (the global average $W_d(R_{0,1}, R_{0,1})$); dashed versus dotted in Fig 5d). In this ‘check’, we did the same analysis as in $R_{0,1}$, but with a 1.5 day shift of the particle release times. As a result, the particle distributions will be different in the check, but as similar as one could get to the particle distributions of $R_{0,1}$ in the other configurations.

On the other hand, altering the spatial resolution in R_{1m} and R_{1md} does lead to different values of the W_d . We find that any value of $c_s > 0$ reduces the W_d by a similar amount, but the W_d is the smallest for $c_s = 2$ with both sinking speeds $w_f = 6, 25 \text{ m day}^{-1}$ (Fig 5d). For $c_s = 2$, the approximated zonal and meridional standard deviation

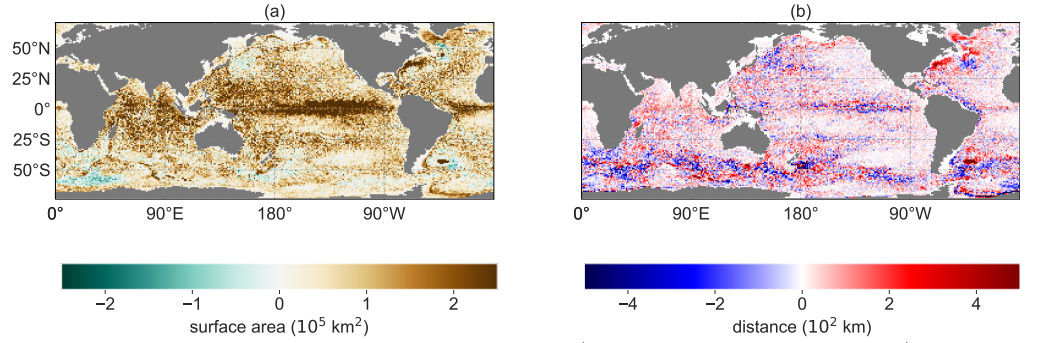


Fig 4. The differences between $R_{0.1m}$ and $R_{0.1}$ ($R_{0.1m}$ subtracted from $R_{0.1}$) in terms of (a) the surface area of the particle distributions (Fig 1c) and (b) the average travel distances of the particle distributions (Fig 1b).

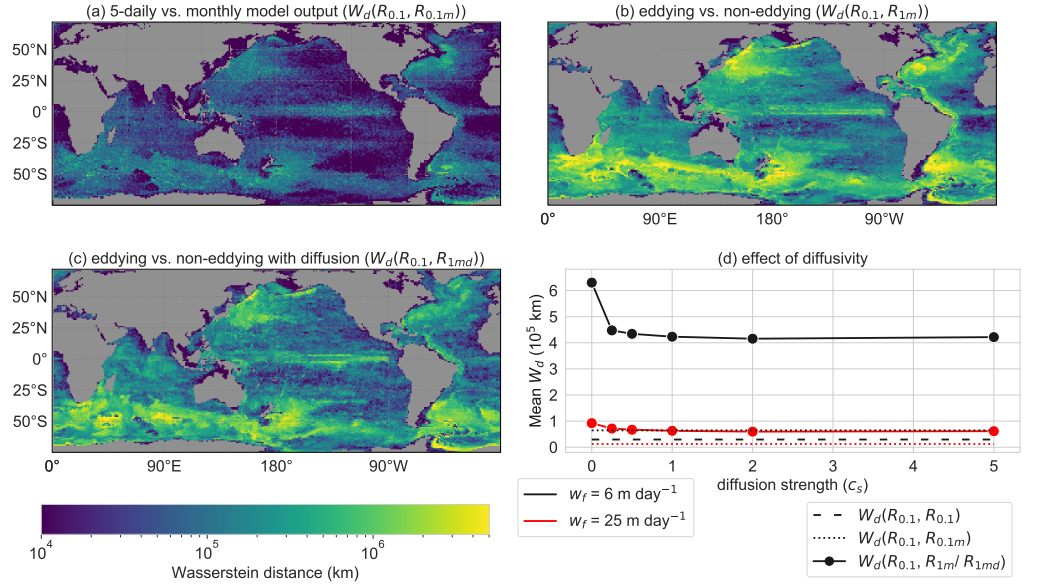


Fig 5. The global Wasserstein distance (W_d) as a distance measure between the back-tracked particle distributions of the configurations from table 1. W_d for sinking speed $w_f = 6 \text{ m day}^{-1}$ between the eddying reference configuration $R_{0.1}$ and (a) the eddying $R_{0.1m}$ with monthly model output, (b) the non-eddying R_{1m} , (c) the non-eddying R_{1md} with diffusion strength $c_s = 2$. (d) Global average W_d in all configurations (for several diffusion strengths c_s in R_{1md}). $w_f = 6 \text{ m day}^{-1}$ in black and $w_f = 25 \text{ m day}^{-1}$ in red. The globally averaged W_d of configuration $R_{0.1}$ with itself is a check ($W_d(R_{0.1}, R_{0.1})$); only for $w_f = 6 \text{ m day}^{-1}$, as the globally averaged W_d is shown between the particle distribution of the same configuration, but with a 1.5-day shift of the particle release times.

of the diffusion ($\hat{\sigma}_x(t)$, $\hat{\sigma}_y(t)$) ranges between 8km and 80km in 20 days (depending on the strength of the local velocity gradients in the model). At this value of c_s , the magnitude of the fluctuations from the eddies lead to the optimal parameterisation, such that the particle distributions spread enough to better match with the particle distributions in the reference case. However, we find that the global averaged W_d for $c_s = 2$ is approximately eight times larger compared to the check ($W_d(R_{0.1}, R_{0.1})$) for $w_f = 6 \text{ m day}^{-1}$, which implies that the particle distributions differ substantially from the reference case. In all configurations R , $W_d(R_{0.1}, R)$ is lower in areas where the

divergence of particle trajectories is relatively small, such as areas of relatively low eddy kinetic energy (e.g. in the gyres; see supporting information), and in areas where the travel time of the particles is relatively short because of the shallow bathymetry (or the particles sink faster).

Regional analysis

In general, the particle trajectories in the lower spatial resolution configuration R_{1m} without diffusion are different compared to the trajectories in the reference configuration $R_{0.1}$, because these trajectories lack the fluctuations provided by eddies and hence they spread less. The only trajectory spread in the non-eddy R_{1m} is caused by flow variability on a larger timescale, such as seasonality. We focus here on some specific locations to see how this can lead to different particle distributions.

If Smagorinsky diffusion is added to the dynamics of the flow (R_{1md}), the fluctuations from the eddies are parameterised and the trajectories spread more. The North Pacific gyre is a location where this parameterisation works well (Fig 6a). Within the gyre, the diffusion is relatively low in the reference configuration and the eddies spread the particle trajectories uniformly in all directions. Adding fluctuations to the flow field in R_{1md} using stochastic noise captures the spread of these eddies in $R_{0.1}$ well. Occasionally the parameterisation also works well in locations with larger shear and eddy activity compared to the North Pacific gyre. For example, for a location in the Antarctic Circumpolar Current (ACC, Fig 6b), the mean flow field (averaged over 6 years) in R_{1m} is similar to the mean flow field in $R_{0.1}$. The stochastic noise can again adequately capture the effect of fluctuations provided by the eddies on the particle distributions.

However, it is well known that non-eddy OGCMs do not get the mean flow field right in all of the locations, because the eddies influence the mean flow field through rectification [70]. The Agulhas region is such an example where the mean flow field is different in R_{1m} compared to the reference case $R_{0.1}$ (Fig 6c). The analysis in R_{1md} provides a particle distribution which only comprises a subset of the particle distribution from the analysis in $R_{0.1}$. If the strength of the noise (c_s) is increased here, at most the spread of the particle distribution increases, but one will not find that any particle originates from the area around Madagascar.

Finally, the addition of spatially dependent noise has one more unrealistic property: The particles tend to artificially accumulate in areas with relatively low horizontal gradients, and hence weak stochastic noise [50–52]. A result of this effect can be found in another location near the ACC, South of Australia (Fig 6d). At this location, configuration R_{1md} results in two clusters of particles, which are separated by an area with high shear, and where the noise is large, while the particles in the reference configuration $R_{0.1}$ clearly form one (more connected) distribution.

Discussion

We assessed the variations of Lagrangian trajectories of sinking particles in flow fields which were generated by OGCMs of different resolutions. We released sinking particles at the bottom of the ocean, tracked them backwards in time until they reached the surface, and investigated how the particle distributions at the ocean surface depend on the OGCM resolution.

If the model output of the high-resolution OGCM is averaged from 5-daily to monthly data, the particle tracking analysis provides similar results in most cases. However, in some specific regions with large shear, we find notable differences of the back-tracked particle distributions at the ocean surface.

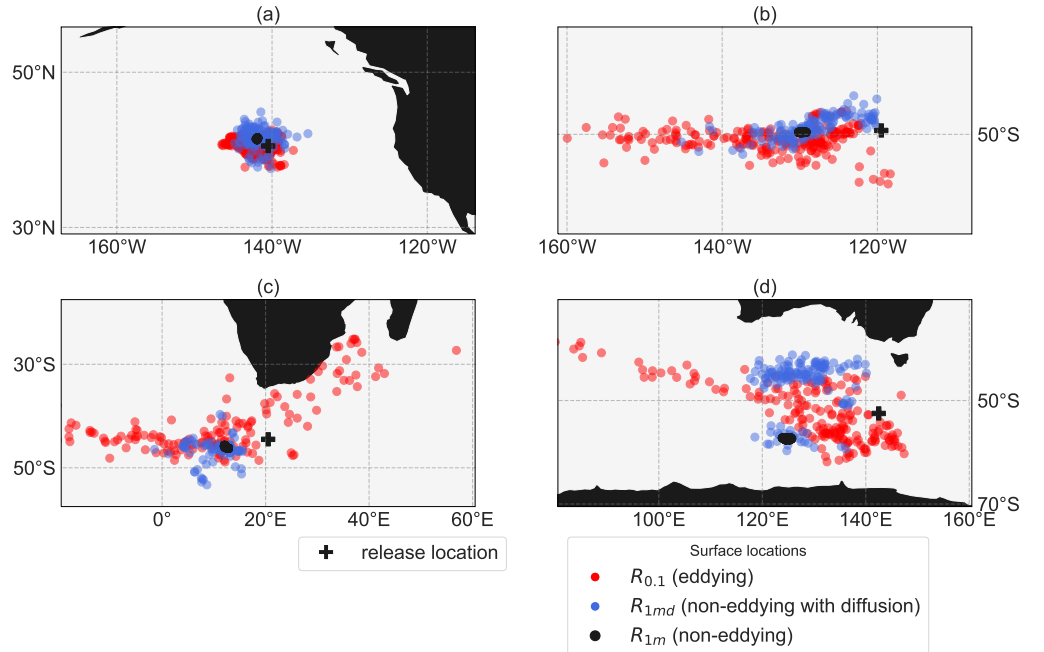


Fig 6. Comparison between reference configuration $R_{0.1}$ (red), configurations R_{1m} (yellow) and R_{1md} with $c_s = 2$ (blue) at four different locations (yellow on top of blue, blue on top of red; $w_f = 6 \text{ m day}^{-1}$). Each distribution consists of ~ 160 particles. The release locations at (a) 40.5°N , 140.5°W and respectively 4601 and 4542 m depth in $R_{0.1}$ and R_{1m} , (b) 49.5°S , 119.5°W and respectively 3122 and 3249 m depth in $R_{0.1}$ and R_{1m} , (c) 44.5°S , 20.5°E and respectively 4249 and 4249 m depth in $R_{0.1}$ and R_{1m} , (d) 52.5°S , 142.5°E and respectively 3070 and 2916 m depth in $R_{0.1}$ and R_{1m}

Overall, the sinking Lagrangian particles give unrealistic results in the non-eddy models, because (1) the back-tracked distributions show too little spread due to the absence of ocean eddies and (2) these models often do not capture the mean flow fields correctly (as shown in e.g. [30, 31, 34]). Lateral stochastic diffusion in the low-resolution configuration (re-)introduced part of the eddy fluctuations and hence increased the relative dispersion of particle trajectories, and increased the lateral travel distance (Fig 2) and the spread (Fig 3) of the back-tracked particle distributions. Hence this method is promising for locations where the low resolution OGCMs capture the mean flow field well. However, the particle distributions are often distant from the distributions of the reference configuration, as is shown from the Wasserstein distance in Fig 5, which implies that the surface origin location is different between the coarse and high resolution models. Therefore, overall the Smagorinsky diffusion is insufficient to parameterise the eddies in most areas.

Altogether, we recommend to compute the sinking Lagrangian particle trajectories only in eddy OGCMs. We used the Smagorinsky parameterisation in this paper as a first attempt to represent the subgrid-scale processes if the eddies are absent in the flow. Other types of parameterisations could be applied. Several other parameterisations for eddy-induced mixing of tracers are available in POP [53]. However, the improvement of either the Eulerian or Lagrangian parameterisation of the subgrid scale variability in the flow remains a challenge in ocean modelling [54].

These conclusions have implications for Lagrangian particles in paleoceanographic models. OGCMs used in most paleo studies lack the eddy flow characteristics and do not generate a locally representative time mean flow for the time period of interest.

Since Lagrangian particles use the local flow field, they require eddying paleoceanographic models that better represent the time mean flow for the considered time period. For the application of Lagrangian particle tracking techniques in paleoceanographic models, which are usually not eddying, we recommend to test model results first against independent information of ocean flow, such as biogeographic patterns of microplankton [55,56]. In turn, it should be appreciated that a regional paleoceanographic signal could be influenced by flow characteristics which are not represented by the non-eddy models. This represents a cautionary tale in putting too much confidence in flow fields from low-resolution fully coupled GCM simulations.

Future work could investigate the sinking Lagrangian particles in other configurations with different OGCM resolutions. The model output of configuration $R_{0.1}$ could be coarsened to a 1° grid before the back-tracking analysis, to separate out the effects on the Lagrangian analysis of (a) a coarsened grid (see also [60,61]) and (b) a lower resolution of the underlying Eulerian model. Moreover, particle trajectories could be sensitive to the vertical resolution of the OGCM (e.g. [3,4]).

When models do not resolve the so-called internal Rossby deformation radius (about 50 km at midlatitudes), no eddies can be represented. When the model grid scale is only slightly smaller than the deformation radius, say 25 km at midlatitudes, eddies form but their interaction is not fully captured; such a model is called ‘eddy permitting.’ Only for models at about 1 km horizontal midlatitude resolution (so-called eddy-resolving models), eddy interactions are fully resolved. The 10 km resolution POP model, as is used here ($R_{0.1}$), is therefore often called ‘strongly eddying.’ An OGCM of ~ 1 km resolution also has a better representation of the spatial/temporal submesoscale that can be important for sinking Lagrangian particles which represent the carbon flux to the ocean bottom [1]. Although the mesoscale flow contains most of the energy that is responsible for the tracer dispersion [62], submesoscale (1-20km) dynamics have proven to be of importance for the vertical advection of iron in specific regions with strong flow-bathymetric interactions [63]. Future work could analyse the transport of sinking particles in models with higher resolutions, and with models which better represent internal tides [69] or improved interaction of the bottom-flow with topography [68].

The effect of eddies on the flow should be appreciated outside the physical oceanography community. In order to facilitate increased understanding on this matter, interactively disseminate our results, and allow users to self-explore and verify the surface-ocean location of origin for sedimentary particles, we developed the website planktondrift.science.uu.nl containing our results.

We also tested an additional configuration without the bolus velocity in the non-eddy POP model (i.e. the same as R_{1md} and R_{1m} , but where $v_b = \vec{0}$). The results for this configuration are very similar to the results that are obtained in configuration R_{1md} and R_{1m} in this paper. The bolus velocity is weaker compared to the Eulerian flow velocity (typically v_b is approximately 5% of v_a at the surface layer). Parameterisations like GM improve the temperature and salinity distribution in Eulerian models. GM is a type of ‘extra advection’ which assumes that dynamic tracers such as temperature and salinity mix along surfaces of constant potential density [36]. However, GM does not make a relevant difference if Lagrangian particles are applied offline to represent other tracers. The results for this additional configuration can be found and downloaded from the planktondrift.science.uu.nl website.

The website contains the results which are presented in this paper, for every release location in every configuration. Users of the tool can choose a location at the bottom of the ocean, see where the sinking particles originated from for different parameters (e.g. the sinking speed w_f , or the magnitude of the noise c_s), and download these origin locations. The website allows anyone who works with e.g. sedimentary microplankton assemblages or plastic to see how the sinking particles could be displaced laterally, and

what the environment (e.g. sea surface temperature and salinity) is at the displaced location using POP or other OGCMs. Hence, the advection bias [20] of the sedimentary assemblages can be determined in the present-day ocean.

Supporting information

S1 Comparison between the reference configuration $R_{0,1}$ (red) and the temporally averaged configuration $R_{0,1m}$ (blue) at two release locations ($w_f = 6 \text{ m day}^{-1}$). (a) 45.5°S , 39.5°E at 2068m depth (red on top of blue) (b) 46.5°S , 42.5°E at 2238m depth (blue on top of red)

S2 Geographic plot of the time mean eddy kinetic energy at the surface. The eddy kinetic energy is defined as $\frac{1}{2}\overline{u' \cdot u'}$, where the bar denotes the time mean and u' the deviation from the time mean velocity vector u (so $u(\vec{x}, t) = \overline{u}(\vec{x}) + u'(\vec{x}, t)$).

S3 Animation (back in time) of particle back-tracking analysis ($w_f = 6 \text{ m day}^{-1}$) with particle release at the Uruguayan margin (47.9°E and 37.15°S , $\sim 4800\text{m}$ depth). (a) the configuration $R_{0,1}$ with 5-daily model output and (b) the configuration $R_{0,1m}$ with monthly model output.

Acknowledgments

The code used for this work and the results are distributed under the MIT license and can be found at the website https://github.com/pdnootboom/PO_res_error. PN thanks Jasper de Jong and Daan Reijnders for their help with the implementation of the Smagorinsky parameterisation in Parcels.

References

1. Philip W. Boyd, Claustre Herve, Marina Levy, David A Siegel, and Thomas Weber. Multi-faceted particle pumps drive carbon sequestration in the ocean. *Nature*, 568:327–335, 2019.
2. Zhan Su, Jinbo Wang, Patrice Klein, Andrew F Thompson, and Dimitris Menemenlis. Ocean submesoscales as a key component of the global heat budget. *Nat. Commun.*, 9(775):1–8, 2018.
3. K D Stewart, A Mcc Hogg, S M Griffies, A P Heerdegen, M L Ward, P Spence, and M H England. Vertical resolution of baroclinic modes in global ocean models. *Ocean Model.*, 113:50–65, 2017.
4. Annalisa Bracco, Jun Choi, Jaison Kurian, and Ping Chang. Vertical and horizontal resolution dependency in the model representation of tracer dispersion along the continental slope in the northern Gulf of. *Ocean Model.*, 122(December 2017):13–25, 2018.
5. Buesseler KO, Antia AN, Chen M, Fowler SW, Gardner WD, Gustafsson O, et al. An assessment of the use of sediment traps for estimating upper ocean particle fluxes. *J Mar Res.* 2007;65:345–416.
6. Weyl PK. Micropaleontology and ocean surface climate. *Science* (80-). 1978;202:475–481.

7. Honjo S, Spencer DW, Farrington JW. Deep Advective Transport of Lithogenic Particles in Panama Basin. *Science* (80-). 1982;216:516–518.
8. Fahl K, Nöthing E.M. Lithogenic and biogenic particle fluxes on the Lomonosov Ridge (central Arctic Ocean) and their relevance for sediment accumulation : Vertical vs . lateral transport. *Deep Res Part 1*. 2007;54:1256–1272. doi:10.1016/j.dsr.2007.04.014.
9. Dale, B.. Palynology principles and applications. In: *Palynol. Princ. Appl.*; 1996. p. 1249–1275.
10. Jalón-Rojas I, Wang Xh, Fredj E. Technical note : On the importance of a three-dimensional approach for modelling the transport of neustic microplastics. *Ocean Sci*. 2019;15:717–724.
11. Kooi M, Nes EHV, Scheffer M, Koelmans AA. Ups and Downs in the Ocean: Effects of Biofouling on Vertical Transport of Microplastics. *Environ Sci Technol*. 2017;51:7963–7971. doi:10.1021/acs.est.6b04702.
12. Koelmans AA, Kooi M, Law KL, van Sebille E. All is not lost: deriving a top-down mass budget of plastic at sea. *Environ Res Lett*. 2017;12.
13. van Sebille E, Griffies SM, Abernathey R, Adams TP, Berloff P, Biastoch A, et al. Lagrangian ocean analysis: Fundamentals and practices. *Ocean Model*. 2018;121(July 2016):49–75. doi:10.1016/j.ocemod.2017.11.008.
14. Zhongfeng Q, Doglioli AM, Carlotti F. Using a Lagrangian model to estimate source regions of particles in sediment traps. *Sci China Earth Sci*. 2014;57(10):2447–2456. doi:10.1007/s11430-014-4880-x.
15. Siegel DA, Deuser WG. Trajectories of sinking particles in the Sargasso Sea: modeling of statistical funnels above deep-ocean sediment traps. *Deep Res 1*. 1997;44(9):1519–1541.
16. Siegel DA, Fields E, Buesseler KO. A bottom-up view of the biological pump : Modeling source funnels above ocean sediment traps. *Deep Res Part 1*. 2008;55:108–127. doi:10.1016/j.dsr.2007.10.006.
17. Monroy P, Drótos G, Hernández-García E, López C. Spatial Inhomogeneities in the Sedimentation of Biogenic Particles in Ocean Flows: Analysis in the Benguela Region. *J Geophys Res Ocean*. 2019;124(May):1–19. doi:10.1029/2019JC015016.
18. Waniek J, Koeve W, Prien RD. Trajectories of sinking particles and the catchment areas above sediment traps in the northeast. *J Mar Res*. 2000;58:983–1006. doi:10.1357/002224000763485773.
19. van Sebille E, Scussolini P, Durgadoo JV, Peeters FJC, Biastoch A, Weijer W, et al. Ocean currents generate large footprints in marine palaeoclimate proxies. *Nat Commun*. 2015;6:6521. doi:10.1038/ncomms7521.
20. Nootboom PD, Bijl PK, Sebille EV, Von Der Heydt AS, Dijkstra HA. Transport Bias by Ocean Currents in Sedimentary Microplankton Assemblages : Implications for Paleoceanographic Reconstructions. *Paleoceanogr Paleoclimatology*. 2019;34. doi:10.1029/2019PA003606.
21. Hardesty BD, Harari J, Isobe A, Lebreton L, Maximenko N, Potemra J, et al. Using Numerical Model Simulations to Improve the Understanding of Micro-plastic Distribution and Pathways in the Marine Environment. *Front Mar Sci*. 2017;4(March):1–9. doi:10.3389/fmars.2017.00030.

22. Baatsen MLJ, von der Heydt AS, Kliphuis M, Viebahn J, Dijkstra HA. Multiple states in the late Eocene ocean circulation. *Glob Planet Change*. 2018;163(February):18–28. doi:10.1016/j.gloplacha.2018.02.009.
23. Hutchinson DK, Boer AMD, Coxall HK, Caballero R, Nilsson J, Baatsen M. Climate sensitivity and meridional overturning circulation in the late Eocene using GFDL CM2 . 1. *Clim Past*. 2018;14(2016):789–810.
24. Baatsen M, von der Heydt AS, Huber M, Kliphuis MA, Bijl PK, Sluijs A, et al. Equilibrium state and sensitivity of the simulated middle-to-late Eocene climate. *Clim Past Discuss*. 2018;(April):1–49. doi:10.5194/cp-2018-43.
25. Lunt DJ, Jones TD, Heinemann M, Huber M, Legrande A, Winguth A, et al. A model – data comparison for a multi-model ensemble of early Eocene atmosphere – ocean simulations: EoMIP. *Clim Paste*. 2012;8:1717–1736. doi:10.5194/cp-8-1717-2012.
26. Haywood AM, Hill DJ, Dolan AM, Bragg F, Chan W, Chandler MA, et al. Large-scale features of Pliocene climate: results from the Pliocene Model Intercomparison Project. *Clim Past*. 2013;9:191–209. doi:10.5194/cp-9-191-2013.
27. Valdivieso Da Costa M, Blanke B. Lagrangian methods for flow climatologies and trajectory error assessment. *Ocean Model*. 2003;6:335–358. doi:10.1016/S1463-5003(03)00023-4.
28. Qin X, van Sebille E, Sen Gupta A. Quantification of errors induced by temporal resolution on Lagrangian particles in an eddy-resolving model. *Ocean Model*. 2014;76:20–30. doi:10.1016/j.ocemod.2014.02.002.
29. Liu G, Bracco A, Passow U. The influence of mesoscale and submesoscale circulation on sinking particles in the northern Gulf of Mexico. *Elem Sci Athropocene*. 2018;6(36).
30. Holland WR. The role of mesoscale eddies in the general circulation of the ocean - Numerical experiments using a wind-driven quasi-geostrophic model. *Am Meteorol Soc*. 1978;8:363–392.
31. Berloff P, Hogg AM, Dewar W. The Turbulent Oscillator : A Mechanism of Low-Frequency Variability of the Wind-Driven Ocean Gyres. *Am Meteorol Soc*. 2007;37:2363–2386. doi:10.1175/JPO3118.1.
32. Penduff T, Juza M, Barnier B, Zika J, Dewar W, Treguier AM, et al. Sea Level Expression of Intrinsic and Forced Ocean Variabilities at Interannual Time Scales. *J Clim*. 2011;24:5652–5670. doi:10.1175/JCLI-D-11-00077.1.
33. Bars DL, Viebahn JP, Dijkstra HA. A Southern Ocean mode of multidecadal variability. *Geophys Res Lett*. 2016;43:2102–2110. doi:10.1002/2016GL068177.
34. Hecht MW, Smith RD. A Review of North Atlantic Ocean Modeling in an Eddying Regime. *Geophys Monogr Ser*. 2013;177:108–109. doi:10.1029/177GM15.
35. Gent PR, McWilliams JC. Isopycnal mixing in ocean circulation models. *J Phys Oceanogr*. 1990;20:150–155.
36. Gent PR. The Gent – McWilliams parameterization : 20 / 20 hindsight. *Ocean Model*. 2011;39:2–9. doi:10.1016/j.ocemod.2010.08.002.

37. Volkov DL, Lee T, Fu LL. Eddy-induced meridional heat transport in the ocean. *Geophys Res Lett*. 2008;35(20):1–5. doi:10.1029/2008GL035490.
38. Viebahn JP, von der Heydt AS, Le Bars D, Dijkstra HA. Effects of Drake Passage on a strongly eddying global ocean. *Paleoceanography*. 2016;31(5):564–581. doi:10.1002/2015PA002888.
39. Smagorinsky J. General circulation experiments with the primitive equations. *Mon Weather Rev*. 1963;91(3):99–163.
40. Weijer W, Maltrud ME, Hecht MW, Dijkstra HA, Kliphuis MA. Response of the Atlantic Ocean circulation to Greenland Ice Sheet melting in a strongly-eddying ocean model. *Geophys Res Lett*. 2012;39(9):1–6. doi:10.1029/2012GL051611.
41. den Toom M, Dijkstra HA, Weijer W, Hecht MW, Maltrud ME, van Sebille E. Response of a Strongly Eddying Global Ocean to North Atlantic Freshwater Perturbations. *J Phys Oceanogr*. 2014;44(2):464–481. doi:10.1175/JPO-D-12-0155.1.
42. Monroy P, Hernández-García E, Rossi V, López C. Modeling the dynamical sinking of biogenic particles in oceanic flow. *Nonlinear Process Geophys*. 2017;24(2):293–305.
43. Delandmeter P, van Sebille E. The Parcels v2.0 Lagrangian framework: new field interpolation schemes. *Geosci Model Dev*. 2019;12:3571–3584.
44. Anderson DM, Lively JJ, Reardon EM, Price Ca. Sinking characteristics of dinoflagellate cysts. *Limnol Oceanogr*. 1985;30(5):1000–1009. doi:10.4319/lo.1985.30.5.1000.
45. Nowald N, Fischer G, Iversen MH, Wefer G. In-situ sinking speed measurements of marine snow aggregates acquired with a settling chamber mounted to the Cherokee ROV. *IEEE Xplore*. 2009;(June). doi:10.1109/OCEANSE.2009.5278186.
46. Jochum M, Danabasoglu G, Holland M, Kwon YO, Large WG. Ocean viscosity and climate. *J Geophys Res*. 2008;113:1–24. doi:10.1029/2007JC004515.
47. Ma J, Wang F, Tang X. Comparison of Several Subgrid-Scale Models for Large-Eddy Simulation of Turbulent Flows in Water Turbine. In: Xu J, Wu Y, Zhang Y, Zhang J, editors. *Fluid Machinery and Fluid Mechanics*. Berlin, Heidelberg: Springer Berlin Heidelberg; 2009. p. 328–334.
48. Gill AE. Instabilities, fronts and the general circulation. In: *Atmosphere-ocean dynamics*, San Diego: Academic press; 1983.
49. Flamary R, Courty N. POT Python Optimal Transport library; 2017. Available from: <https://github.com/rflamary/POT>.
50. Visser AW. Using random walk models to simulate the vertical distribution of particles in a turbulent water column. *Mar Ecol Prog Ser*. 1997;158:275–281.
51. Hunter JR, Craig PD, Phillips HE. On the Use of Random Walk Models with Spatially Variable Diffusivity. *J Comput Phys*. 1993;106:366–376.
52. Ross ON, Sharples J. Recipe for 1-D Lagrangian particle tracking models in space-varying diffusivity. *Limnol Oceanogr Methods*. 2004; p. 289–302.

53. Smith R, Jones P, Briegleb F, Bryan F, G D, Dennis J, et al. The Parallel Ocean Program (POP) Reference Manual Ocean Component of the Community Climate System Model (CCSM) and Community Earth System Model (CESM). LAUR-01853. 2010;141.
54. Fox-Kemper B, Adcroft A, Böning CW, Chassignet EP, Gerdes R, Greatbatch RJ, et al. Challenges and Prospects in Ocean Circulation Models. *Front Mar Sci.* 2019;6(February):1–29. doi:10.3389/fmars.2019.00065.
55. Huber M, Brinkhuis H, Stickley CE, Do K. Eocene circulation of the Southern Ocean : Was Antarctica kept warm by subtropical waters ? *Paleoceanography.* 2004;19:1–12. doi:10.1029/2004PA001014.
56. Bijl PK, Pross J, Warnaar J, Stickley CE, Huber M, Guerstein R, et al. Environmental forcings of Paleogene Southern Ocean dinoflagellate biogeography. *Paleoceanography.* 2011;26(1):1–12. doi:10.1029/2009PA001905.
57. Claudia Wekerle, Thomas Krumpen, Tilman Dinter, Wilken-jon von Appen, Morten Hvitfeldt Iversen, and Ian Salter. Properties of Sediment Trap Catchment Areas in Fram Strait : Results From Lagrangian Modeling and Remote Sensing. *Front. Mar. Sci.*, 5(November), 2018.
58. Kristofer Döös, Volfrango Rupolo, and Laurent Brodeau. Dispersion of surface drifters and model-simulated trajectories. *Ocean Model.*, 39:301–310, 2011.
59. Magne Simonsen, Øyvind Saetra, Pål Erik, Ole Christian, Hilde Kristin, Brit Salbu, Hilde Elise Heldal, and Justin P Gwynn. The impact of tidal and mesoscale eddy advection on the long term dispersion of 99Tc from Sellafield. *J. Environ. Radioact.*, 177:100–112, 2017.
60. Helga S Huntley, B.L. Lipphardt Jr., and A.D. Kirwan jr. Lagrangian predictability assessed in the East China Sea. *Ocean Model.*, 36(1-2):163–178, 2011.
61. Nathan Putman and Ruoying He. Tracking the long-distance dispersal of marine organisms : Sensitivity to ocean model resolution. *J. R. Soc. Interface*, 10(February 2016), 2013.
62. Takaya Uchida, Dhruv Balwada, Ryan Abernathey, Galen McKlinley, Shafer Smith, and Marina Levy. The Contribution of Submesoscale over Mesoscale Eddy Iron Transport in the Open Southern Ocean. *J. Adv. Model. earth Syst.*, 11:3934–3958, 2019.
63. Isabella Rosso, Andrew Mcc, Richard Matear, and Peter G Stratton. Deep-Sea Research I Quantifying the influence of sub-mesoscale dynamics on the supply of iron to Southern Ocean phytoplankton blooms. *Deep. Res. Part I*, 115:199–209, 2016.
64. J. McClean, S. Jayne, M. Maltrud, and D. Ivanova. The Fidelity of Ocean Models With Explicit Eddies. In M.W. Hecht and H. Hasumi, editors, *Ocean Model. an Eddy regime*, chapter 2, pages 149–164. American Geophysical Union, Washington, DC, 2008.
65. Lloyd Regier and Henry Stommel. Float trajectories in simple kinematic flows. *Proc. Natl. Acad. Sci.*, 76(10):4760–4764, 1979.
66. Geoffrey Gebbie and Peter Huybers. How is the ocean filled ? *Geophys. Res. Lett.*, 38(February):1–5, 2011.

67. Robert Hallberg. Using a resolution function to regulate parameterizations of oceanic mesoscale eddy effects. *Ocean Model.*, 72:92–103, 2013.
68. Elda Miramontes, Pierre Garreau, Matthieu Caillaud, Gwenael Jouet, Romain Pellen, F Javier Hernández-molina, Michael A Clare, and Antonio Cattaneo. Contourite distribution and bottom currents in the NW Mediterranean Sea : Coupling seafloor geomorphology and hydrodynamic modelling. *Geomorphology*, 333:43–60, 2019.
69. Clément Vic, Alberto C Naveira Garabato, J A Mattias Green, Amy F Waterhouse, Zhongxiang Zhao, Angélique Melet, Casimir De Lavergne, Maarten C Buijsman, and Gordon R Stephenson. Deep-ocean mixing driven by small-scale internal tides. *Nat. Commun.*, 10(2099), 2019.
70. Piergianluca Porta Mana and Laure Zanna. Toward a stochastic parameterization of ocean mesoscale eddies. *Ocean Model.*, 79:1–20, 2014.